ACADEMIC PRESS

Available online at www.sciencedirect.com

SCIENCE DIRECT®

Journal of Sound and Vibration 269 (2004) 1031–1062

JOURNAL OF SOUND AND VIBRATION

www.elsevier.com/locate/jsvi

# Development of high bandwidth powered resonance tube actuators with feedback control

G. Raman[a,*], S. Khanafseh[a], A.B. Cain[b], E. Kerschen[c]

[a] *Mechanical, Materials and Aerospace Engineering Department, Illinois Institute of Technology, 10 West 32nd Street, Chicago, IL 60616, USA*

[b] *Innovative Technology Applications Company, LLC, P.O. Box 6971, Chesterfield, MO 63006-6971, USA*

[c] *Department of Aerospace and Mechanical Engineering, University of Arizona, Tucson, AZ 85721, USA*

Received 9 August 2002; accepted 24 January 2003

**Abstract**

A high bandwidth powered resonance tube (PRT) actuator potentially useful for noise and flow control applications was developed. High bandwidth allows use of the same actuator at various locations on an aircraft and over a range of flight speeds. The actuator selected for bandwidth enhancement was the PRT actuator, which is an adaptation of the Hartmann whistle. The device is capable of producing high-frequency and high-amplitude pressure and velocity perturbations for active flow control applications. Our detailed experiments aimed at understanding the PRT phenomenon are complemented by an improved analytical model and direct numerical simulations. We provide a detailed characterization of the unsteady pressures in the nearfield of the actuator using phase averaged pressure measurements. The measurements revealed that propagating fluctuations at 9 kHz were biased towards the upstream direction (relative to the supply jet). A complementary computational study validated by our experiments was useful in simulating the details in the region between the supply jet and the resonance tube where it was difficult to gather experimental data. High bandwidth was obtained by varying the depth of the resonance tube that determines the frequency produced by the device. Our actuator could produce frequencies ranging from 1600 to 15,000 Hz at amplitudes as high as 160 dB near the source. The frequency variation with depth is predicted well by the quarter wavelength formula for deep tubes but the formula becomes increasingly inaccurate as the tube depth is decreased. An improved analytical model was developed, in which the compliance and mass of the fluid in the integration slot is incorporated into the prediction of resonance frequencies of the system. Finally a feedback controller that varied both the resonance tube depth and spacing to converge on a desired frequency was developed and demonstrated. We are optimistic that numerous potential applications exist for such high bandwidth high dynamic range actuators.


*Corresponding author. Tel.: +312-567-3554; fax: +312-567-3173.
*E-mail address:* raman@iit.edu (G. Raman).

0022-460X/03/$ - see front matter © 2003 Published by Elsevier Science Ltd.
doi:10.1016/S0022-460X(03)00212-8

## 1. Introduction

High-bandwidth actuation is essential for the effective application of active flow control (AFC) to improve the efficiency of systems that involve both internal and external fluid flow. Successful application to aircraft systems can produce lighter, stealthier, agile aircraft with increased range, payload and a muffled acoustic signature. The design of an AFC system requires knowledge of flow phenomena and selection of appropriate actuators, sensors, and a control algorithm. The present paper focuses on the development of high-bandwidth actuators for active flow and noise control applications. It should be noted that the powered resonance tube (PRT) derives its name from the Hartmann resonance tube. The term 'powered' indicates that both 'unpowered' (deriving energy from the free stream) and 'powered' (requiring secondary air) versions are possible. The term 'bandwidth' refers to the range of frequencies of effective operation. Our goal is to demonstrate a PRT that can generate strong tones over a frequency 'bandwidth' of approximately one order of magnitude, and is done as a part of the USAF's program on 'high-bandwidth actuators.' Thus, it should be noted that the term 'bandwidth' is not intended to convey an instantaneous output state but rather the range of conditions over which the device is applicable.

AFC techniques can be separated into two classes based on flow physics [1]. The first class (AFC-I) involves the use of unsteady forcing to excite instability waves of laminar flows, or the large-scale structures of turbulent flows. AFC-I techniques have been explored extensively in the past decade [2,3]. The second class (AFC-II), that has been developed more recently, involves the use of actuators to force turbulent boundary and free-shear layers at high frequencies in the Kolmogorov inertial subrange (see Refs. [4,1]). Our quest for a high-bandwidth actuator is preceded by the recognition that the two classes of AFC have different bandwidth requirements, as discussed below.

To effect AFC across the full operating envelope of an air vehicle, actuators with high bandwidth and large dynamic range are required. To illustrate this consider the actuator bandwidth requirements for a military transonic air vehicle. For this illustration we assume that the minimum and maximum speeds of interest for tactical military aircraft differ by a factor of eight. We also assume that the streamwise locations of interest for actuators vary by a factor of eight. Further reasoning is based on an estimate of the boundary layer thickness, which for laminar boundary layers scales with the square root of the downstream distance, $X$ and the inverse square root of the flow speed $U$. The thickness of the turbulent boundary layer scales roughly with the $\frac{6}{7}$ power of the downstream distance, $X$ and the $\frac{1}{7}$ power of the flow speed, $U$. AFC-I techniques have more stringent requirements and the actuator must produce an unsteady flow disturbance at a frequency that is near the frequency of the naturally occurring instability waves or large-scale structures. The required frequency scales as $f \alpha U/\delta$. Thus, for a laminar boundary layer we obtain $f \alpha U^{3/2} X^{-1/2}$, while for a turbulent boundary layer we obtain $f \alpha U^{8/7} X^{-6/7}$. Now consider an actuator on a fixed location on a vehicle. In order for the actuator to be effective for AFC-I over a speed range of 8, a bandwidth range of $8^{3/2} \approx 23$ would be required for a laminar boundary layer, while a bandwidth range of $8^{8/7} \approx 11$ would be required for a turbulent boundary layer. In reality the laminar scaling overestimates the requirement in many situations, since one would anticipate a significant shift in transition location over a speed range of 8. Thus, for AFC-I techniques, a reasonable estimate for the desired bandwidth range for an

actuator at a fixed location is, say 16. We can also consider the possibility of AFC-I applications using the same actuator at all locations on a vehicle. In this case the desired bandwidth range increases to 64, for both laminar and turbulent cases.

AFC-II techniques involve excitation of disturbances in the inertial subrange of the turbulent boundary layer or free-shear layer. Here the bandwidth requirements are more modest. The instability modes or large-scale structures that are excited in AFC-I have a fairly narrow frequency band (at a given point in the boundary or free shear layer). In contrast, the inertial subrange of a turbulent layer typically extends over a frequency range of say an order of magnitude. It is only necessary to force the turbulent flow at some frequency within this range. Therefore for AFC-II techniques, the possibility of effecting flow control using the same actuator at a variety of locations on a vehicle appears realistic.

### 1.1. Background on actuators

Several innovative flow control techniques have emerged in recent years. Among these are piezoelectric actuators, zero mass flux actuators [4,5] and fluidic actuators. However, the above types of actuators are suited more for laboratory experiments. In full-scale flight applications they can prove to be fragile and have significant power and maintenance requirements, and may not be able to provide the necessary bandwidth.

Our actuator is based on the Hartman resonance tube (also referred to as the Hartman whistle). The resonance tube phenomenon was first described by Hartmann in 1918 (Hartmann and Troll [6], Hartmann [7]). The Hartmann whistle apparatus consists of a jet aimed at the open end of a tube which is closed at the other end. There are two phases during the operation of this device. In the first phase, the jet penetrates the tube and compresses the air within the tube. In the second phase the compressed air in the tube empties itself. Under favorable conditions the cycle perpetuates itself. However, fixed geometry actuators can only produce effective actuation over a small range of frequencies. This poses a problem because we require a new actuator every time there is a change in geometric or fluid dynamic parameters. Extending earlier fixed frequency efforts [8–10], our goal was to use the oscillatory pressures and velocities produced by this device to design a high-bandwidth actuator. Examples of possible applications include the high-frequency excitation for suppression of flow-induced resonance in weapons bay cavities [8,9,11,12] and jet-ground impingement tones in STOVL aircraft.

The phenomena associated with such resonance tubes has been studied by several researchers including Thompson et al. [13] and Brocher et al. [14]. The resonance frequency was proposed by Brocher et al. [14] to be equal to approximately the acoustic frequency $f = a/(4L + ecf)$, where $f$ is the resonance frequency, $a$ is the ambient speed of sound, $L$ is the length of the tube, and $ecf$ is the end correction factor. Note that the frequency of excitation produced by this device depends primarily on its depth. Secondary factors that can alter frequency include the nozzle pressure ratio (NPR) of the supply nozzle and the spacing between the jet exit and the open end of the resonance tube. A variation of the Hartmann tube known as the Hartmann–Sprenger tube was studied by Iwamoto [15] and Iwamoto and Deckker [16]. Wilson [17] and Wilson and Resler [18] studied a glass resonance tube using pulsed schlieren. Wilson's work documents the movement of waves within the tube during the compression and evacuation phases within the tube and also documents the temperature variations at the closed end of the tube.

### 1.2. Benefits of high-frequency excitation

An additional motivation to develop a high-bandwidth PRT is the need to use high-frequency excitation (AFC-II) for control applications. High-frequency excitation (AFC-II) departs from the conventional philosophy (AFC-I) of exciting the shear layer only within the range of frequencies where the large scale structures (see Ref. [19]) are amplified. The rationale in the conventional excitation approach (AFC-I) was to energize the large structures that in turn enhance mixing. In contrast, when frequencies that are an order of magnitude higher than the large scale range are used, the dissipative scales are excited which in turn can bring about large changes in the development of the large scales and the mean flow (see Ref. [4]). An important consequence of the high-frequency excitation is that the direct addition of dissipative scales apparently accelerates the dynamics of energy cascade across a broad range of wave numbers. In situations involving resonant acoustics, low-frequency excitation reduces the amplitude of resonant tones by detuning the feedback loop. In contrast, high-frequency excitation destroys the organization in the initial shear layer that is necessary to sustain flow-induced resonance. Typically, the use of low-frequency excitation (in the range of naturally amplified flow instabilities) results in the suppression of some modes and is generally accompanied by the augmentation of some other modes. In contrast, high-frequency excitation (AFC-II) has the capability of eliminating all tones present in a cavity in subsonic/supersonic flight. The ability to suppress all tones is especially important in situations where the resonant frequencies are difficult to anticipate. For example, in the work of Raman et al. [20] on jet-cavity interactions two types of tones were observed. The first type was described by $H = 0.3nM_j^{1/2}$ for $n = 1, 2, 3$, where '$H$' is the Helmholtz number given by $fL/a$, where '$f$' is the frequency, '$L$' the cavity length and '$a$' the speed of sound. The second type of tone can be approximated by the relationship $H = (n + 1)/4$ *for* $n = 1, 2, 3$. The former type resembles the Rossiter modes whereas the latter type is independent of cavity length (note that the classical Rossiter modes may occur only in idealized laboratory experiments). The point here is that with conventional low-frequency excitation one needs to know the frequencies of the tones that are expected under various conditions. High-frequency excitation has the potential to suppress all flow-induced resonances and does not require detailed knowledge of the frequencies of tones present under various conditions.

### 1.3. Objectives

Our approach for developing a high-bandwidth actuator consisted of first selecting a candidate actuator and then devising a method to extend its bandwidth. Our search for an actuator revealed that excitation devices that produced high-amplitude signals generally leveraged a resonance mechanism. Examples are piezoelements mounted on structural members, and devices that exhibit aeroacoustic resonance. The former type of actuator (piezo) was considered briefly but was dropped in favor of the latter type (aeroacoustic). The actuator selected for bandwidth enhancement was the PRT actuator, which is capable of producing high-frequency and high-amplitude oscillations.

The frequency produced depends approximately on the quarter wavelength frequency of a tube that is closed at one end. First, we demonstrated that high bandwidth could be produced by manually varying the depth of the PRT. This was followed by a more refined effort using a

computer controlled mechanism that varied the depth of the tube in response to user selected frequencies. We were successful in obtaining an order of magnitude variation in frequency with a significant dynamic range. Specific objectives are characterize the unsteady actuation signals produced by the PRT device in the nearfield; develop and demonstrate high bandwidth capability; begin with a look up table (LUT) approach and proceed to demonstrate single input single output (SISO) and multi input multi output (MIMO) feedback control of the actuator.

## 2. Powered resonance tube development

Fig. 1 shows a schematic of a single PRT. The supply jet is seen on the left-hand side and the resonance tube on the right hand side. Previous work has focused on two versions of the resonance tube. The original version used an underexpanded sonic jet containing a shock train. In the second version Brocher et al. [14] demonstrated that a "wake producing" cylinder laid along the jet axis allows the full oscillation amplitude to be achieved for ideally expanded supersonic jets. Hartmann [7], Wilson [17] and Brocher [14] have pointed out that the former version is very sensitive to spacing between the jet and mouth of the resonance tube. This is because the expanding region of the jet is a stable region for a shock present in the flow, whereas the converging region is unstable, so that the shock will not remain there.

For a resonance tube to operate, the spacing between the nozzle exit and the tube mouth should be such that it positions the shock in the unstable region. When the shock is in the unstable region it is strongly affected by downstream conditions and will readily oscillate. The desired spacing between the nozzle exit and the resonance tube depends on the shock cell dimensions that are determined by the supply pressure. This explains the sensitivity to both spacing and supply pressure. In contrast, in the latter version, the jet is ideally expanded and has no shock cells. However, the sting does generate oscillations with a lower sensitivity to the pressure and spacing. Our work demonstrates that using a properly designed control system even the former version of the resonance tube can produce oscillations consistently. A similar control system is expected to function quite easily for the latter version of the device. Note that although the latter version is less sensitive to supply pressure and spacing it still needs fine tuning to produce the maximum

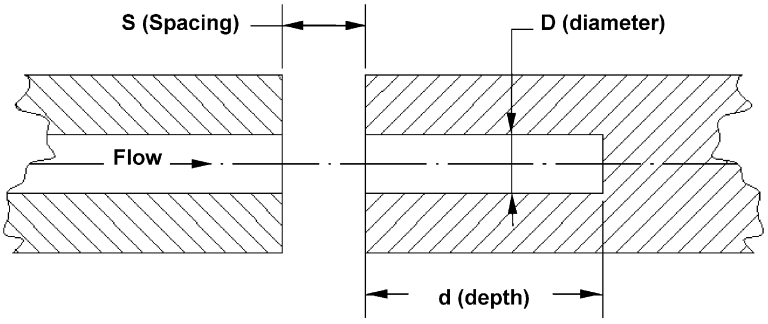


Fig. 1. Schematic diagram showing an axisymmetric PRT. The supply jet is on the left-hand side and the resonance tube is on the right. The gap between the two is referred to as the integration slot (IGS).

amplitude. The frequency of the resonance depends only on the depth of the tube for subsonic or ideally expanded supersonic jets. The distance between the supply jet and the resonance tube determines the efficiency of this process. The mass flow requirements depend on the diameter of the supply jet and typically range from 0.01 kg/s to 0.15 kg/s for tubes with diameters ranging from 0.158 to 0.635 cm.

Although the Hartmann tube has been known for many years it has never been used before as an AFC actuator. Raman et al. [8] demonstrated its potential for use as an AFC actuator. However, the demonstrator was not suitable for use as an actuator since the flow spilled out circumferentially in all directions. For effective actuation a device that can inject perturbations into a flow efficiently is desired. We began integration efforts by using a semi-circular shroud. The shroud or shield (when applied properly) did not alter the effectiveness of the resonance tube phenomenon. Two generations (Gen-I and Gen-II) of a more complex version of this device were developed. The Gen I type actuator, which was designed to integrate with the weapons bay cavity at DERA (UK), was described by Raman et al. [9] and Raman and Kibens [10] and will only be briefly mentioned herein. The actuator consisted of a flow-conditioned plenum fed by a high-pressure air line. The flow exited the plenum through seven supersonic (CD) nozzles with an exit diameter of 0.635 cm and a design Mach number of 2. The seven jet nozzles were aimed at a block containing seven resonance tubes with a diameter of 0.635 cm and a depth of 1.27 cm. An axial needle was present at the center of each of the jet nozzles. The needle enhances the operation of these nozzles at supersonic Mach numbers as originally proposed by Brocher et al. [14] to prevent cessation of oscillations for certain conditions. Also present in the actuator is a scalloped plate spacer between the supply jet and the resonance tube. Stanek et al. [12] describe the results from the cavity noise suppression experiments in the UK. The device suppressed cavity tones by 29 dB at $M = 1.19$.

A second generation device (Gen-II) was built to integrate with the jet impingement apparatus at Boeing Saint Louis. The Gen-II actuator was switchable between 7 and 15 powered resonance tubes and had a bleed facility at the rear that allowed the mass flow to be varied. This actuator was successful in suppressing impingement tones (see Ref. [10]).

### 2.1. Experimental setup

The experimental set-up shown in Fig. 2, consists of a 0.635 cm diameter jet with a chamfered exit facing the open end of the resonance tube that is closed at the other end. Note that the chamfer was necessary for the production of high-amplitude oscillations. A piston fitted inside the tube changes the tube depth. The piston has an O-ring built in to prevent leakage of air. This setup was used as a prototype to test the parameters of the PRT. The piston remained fixed while the resonance tube slid over it to change tube depth. The distance between the jet and the tube (gap), referred to as the ''spacing parameter'' or ''spacing'' was changed by computer control to examine its effect on both the frequency and the amplitude of the sound. Microphones and pressure sensors at various locations in the vicinity of the actuator were used to measure the frequency and amplitude of the fluctuations produced by this device. The power spectrum of the acoustic signal was computed for various resonance tube depths and jet-to-resonance-tube spacings. A computer controlled traversing mechanism moved both the piston (for changing depth) and the supply jet

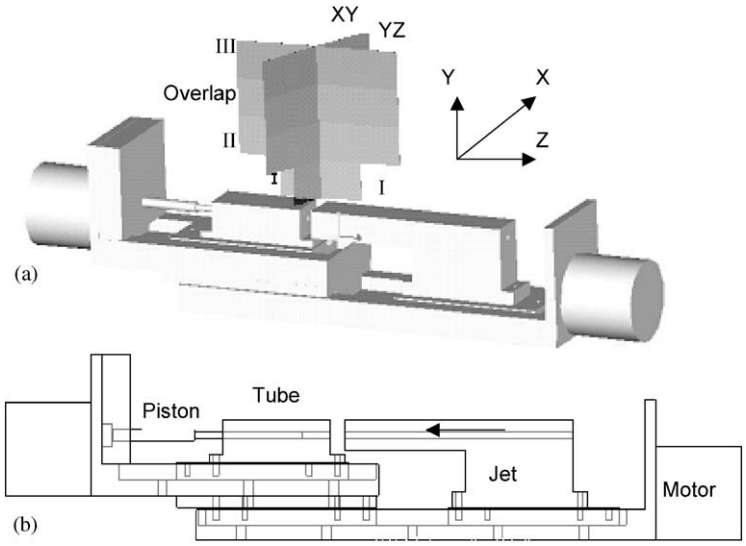


Fig. 2. Schematic diagram of computer controlled high-bandwidth PRT actuator. Measurements planes ($XY$ and $YZ$) were used for the phase-averaged measurements. Planes II and III overlap. (a) Three-dimensional view showing measurement planes. (b) Front view showing details of construction.

for changing the spacing (tuning). We then generated a detailed experimental database that was used as a lookup table for our computer controlled experiment.

### 2.2. Error analysis

There are two types of errors: external and internal. The former is based on a knowledge of the accuracy of the instrumentation while the latter is based on the data and repeatability of the experiment. For the microphone measurement, the only available information is the precision of the microphone. The precision of the microphone provided by the manufacturer is 0.5 dB which results in a microphone measurement error of $\pm 1$ dB based on a zero order estimate, for the frequency range from 0 to 10 kHz. For the Kulite pressure transducer, the calibration sheet provided states that the error is less than $\pm 3\%$. To state the external errors a statistical analysis of the data was needed. Hence numerous measurements were conducted on the PRT to establish the uncertainty, validate our data, and study the repeatability of the experiment. One major objective was to show that the phenomenon is steady and the variation of the resonance amplitude and frequency is within an acceptable range of error bars. This evaluation was represented by a statistically estimated standard deviation $\sigma$ then using a 95% confidence interval of $2\sigma$. These measurements are tabulated in Tables 1 and 2. From Table 1 it can be seen that the frequency error is less than 40 Hz for each case of ascending and descending order with a 70 Hz hysteresis error. While form Table 2 it can be seen that the sound pressure level (SPL) error is 2.24 dB with a hysteresis error of 3.8 dB.

Table 1
Frequency error analysis measurements for PRT

| | Frequency (kHz) | | | | | | | | | | | | $\sigma$ | |
|---|---|---|---|---|---|---|---|---|---|---|---|---|---|---|
| *d*/*D* | Asc.[a] run 1 | Des.[b] run 1 | Asc. run 2 | Des. run 2 | Asc. run 3 | Des. run 3 | Asc. run 4 | Des. run 4 | Asc. run 5 | Des. run 5 | Asc. mean | Des. mean | Asc. | Des. |
| 0.8 | 9.844 | 9.756 | 9.820 | 9.756 | 9.828 | 9.784 | 9.860 | 9.780 | 9.860 | 9.780 | 9.842 | 9.771 | 0.02 | 0.01 |
| 1.2 | 7.764 | 7.692 | 7.760 | 7.704 | 7.768 | 7.700 | 7.772 | 7.704 | 7.780 | 7.708 | 7.769 | 7.702 | 0.01 | 0.01 |
| 1.6 | 6.472 | 6.440 | 6.472 | 6.444 | 6.476 | 6.452 | 6.492 | 6.452 | 6.492 | 6.452 | 6.481 | 6.448 | 0.01 | 0.01 |
| 2.0 | 5.188 | 5.176 | 5.180 | 5.176 | 5.180 | 5.216 | 5.220 | 5.208 | 5.212 | 5.200 | 5.196 | 5.195 | 0.02 | 0.02 |
| 2.4 | 4.260 | 4.236 | 4.256 | 4.240 | 4.260 | 4.240 | 4.260 | 4.240 | 4.264 | 4.240 | 4.260 | 4.239 | 0.00 | 0.00 |
| 2.8 | 3.680 | 3.672 | 3.684 | 3.676 | 3.684 | 3.672 | 3.692 | 3.672 | 3.696 | 3.680 | 3.687 | 3.674 | 0.01 | 0.00 |
| 3.2 | 3.308 | 3.304 | 3.308 | 3.304 | 3.312 | 3.300 | 3.308 | 3.304 | 3.324 | 3.304 | 3.312 | 3.303 | 0.01 | 0.00 |
| 3.6 | 3.008 | 2.992 | 3.008 | 2.996 | 3.008 | 2.996 | 3.008 | 2.996 | 3.012 | 3.000 | 3.009 | 2.996 | 0.00 | 0.00 |
| 4.0 | 2.756 | 2.744 | 2.756 | 2.744 | 2.760 | 2.752 | 2.756 | 2.756 | 2.760 | 2.756 | 2.758 | 2.750 | 0.00 | 0.01 |
| 4.4 | 2.540 | 2.540 | 2.540 | 2.540 | 2.540 | 2.540 | 2.540 | 2.540 | 2.540 | 2.540 | 2.540 | 2.540 | 0.00 | 0.00 |

[a] Asc.: ascending order.
[b] Des: descending order.

Table 2
Amplitude error analysis measurements for PRT

| | SPL (dB) | | | | | | | | | | | | $\sigma$ | |
|---|---|---|---|---|---|---|---|---|---|---|---|---|---|---|
| *d*/*D* | Asc.[a] run1 | Des.[b] run 1 | Asc. run 2 | Des. run 2 | Asc. run 3 | Des. run 3 | Asc. run 4 | Des. run 4 | Asc. run 5 | Des. run 5 | Asc. mean | Des. mean | Asc. | Des. |
| 0.8 | 148 | 147 | 148 | 147 | 148 | 146 | 148 | 147 | 148 | 146 | 148.0 | 146.6 | 0.00 | 0.55 |
| 1.2 | 147 | 151 | 148 | 151 | 148 | 151 | 148 | 151 | 148 | 151 | 147.8 | 151.0 | 0.45 | 0.00 |
| 1.6 | 155 | 153 | 155 | 153 | 155 | 152 | 156 | 154 | 155 | 153 | 155.2 | 153.0 | 0.45 | 0.71 |
| 2.0 | 148 | 144 | 149 | 145 | 148 | 145 | 149 | 144 | 149 | 146 | 148.6 | 144.8 | 0.55 | 0.84 |
| 2.4 | 153 | 149 | 153 | 150 | 154 | 150 | 153 | 150 | 153 | 150 | 153.2 | 149.8 | 0.45 | 0.45 |
| 2.8 | 152 | 148 | 150 | 149 | 149 | 149 | 151 | 150 | 151 | 149 | 150.6 | 149.0 | 1.14 | 0.71 |
| 3.2 | 141 | 139 | 140 | 138 | 142 | 140 | 143 | 139 | 141 | 139 | 141.4 | 139.0 | 1.14 | 0.71 |
| 3.6 | 144 | 146 | 145 | 147 | 146 | 147 | 145 | 148 | 144 | 147 | 144.8 | 147.0 | 0.84 | 0.55 |
| 4.0 | 147 | 143 | 148 | 145 | 145 | 144 | 146 | 145 | 147 | 143 | 146.6 | 144.2 | 1.14 | 1.00 |
| 4.4 | 143 | 144 | 143 | 143 | 144 | 143 | 143 | 144 | 143 | 144 | 143.2 | 143.6 | 0.45 | 0.55 |

[a] Asc.: ascending order.
[b] Des: descending order.

## 3. Experimental results

### 3.1. Frequency and amplitude characteristics

Fig. 3(a) shows the variation of actuator resonance frequency versus depth. In this paper NPR is defined as the ratio of the stagnation pressure to ambient pressure. The data of Fig. 3(a) were

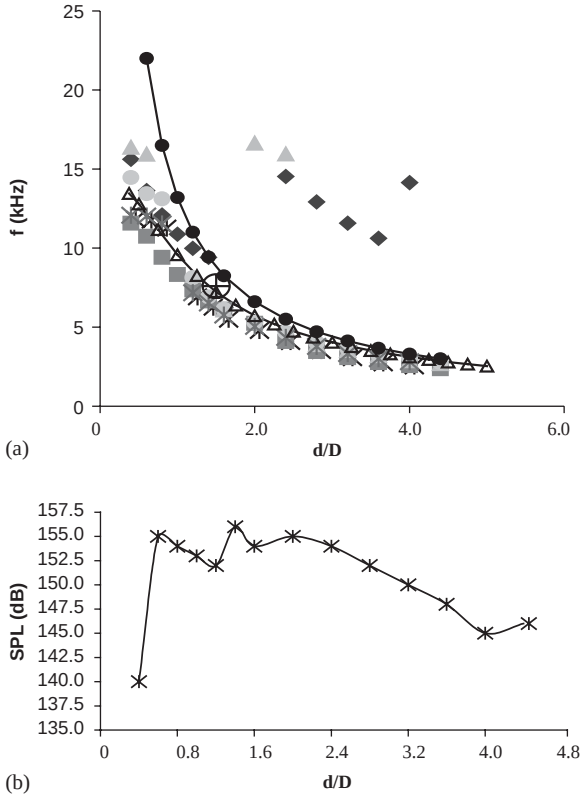


Fig. 3. Frequency and amplitude characteristics of PRTs at an NPR of 3.72 (NPR_Standard = 1.15 NPR). (a) Actuation frequency versus depth for various values of the spacing parameter (jet-to-resonance-tube spacing). (b) Actuation amplitude versus depth for various values of the spacing parameter (jet-to-resonance-tube spacing). ◆, $s/D = 0.8$, ■, $s/D = 1.2$, ▲, $s/D = 1.6$, ●, $s/D = 2.0$, ⁎, $s/D = 2.4$, —●—, QWL theory, ⊕, simulation point at $s/D = 1$ and $d/D = 1.5$ and —△—, Kerschen's theory.

acquired at an NPR of 3.72 for various values of the spacing parameter (integration slot width or jet to resonance tube spacing). Two theoretical predictions of the resonance frequency are also shown in Fig. 3(a). The basic theory is the standard $\frac{1}{4}$ wavelength resonance frequency (QWL), for an open-closed resonance tube. The experimental data are in good agreement with the basic theory for long tube depths, but gradually diverge from the basic theory as the depth of the resonance tube decreases. In order to develop a better understanding of this behavior, we developed a refined theory (Kerschen [21]) that considers the acoustic coupling of the resonance tube and the integration slot. The Kerschen [21] theory accounts for the interaction of the resonance tube with the integration slot, and the compliance and mass of the fluid in the integration slot are incorporated into the prediction. The prediction of this refined theory for an integration slot width of $s/D = 1$ is shown in Fig. 3(a). The refined theory is in much better agreement with the experimental data, remaining quite accurate even at small values of the tube depth. Essentially, for small tube depths, the inertia of the fluid in the integration slot becomes important, significantly reducing the resonance frequency relative to the prediction of the basic theory.

Numerical simulations of the PRT actuator have been carried out for a tube depth of $d/D = 1.5$, an integration slot width of $s/D = 1$, and a supply nozzle pressure ratio (NPR $= p/p$ (ambient)) of 3.5. Details of the simulation are discussed in a later section. A single result from the numerical simulations will be used for comparison with the experimental results in Fig. 3. The resonance frequency obtained in the simulation, $f = 7.6$ kHz, is also shown in Fig. 3(a). The result is seen to be in good agreement with the experimental data and refined theory. The simulation also determines the amplitude of the resonance. Accounting for the pressure scaling discussed above, the simulation result corresponds to an amplitude of 160 dB, in fairly good agreement with the laboratory value of 157 dB.

Note that in the experiments the frequency could be changed from 14 to about 1.6 kHz and amplitude varied from 137 to 160 dB. A documentation of the amplitude of sound at a nearfield microphone location (0.635 cm away from the PRT) with varying resonance tube depth (various frequencies) is provided in Fig. 3(b). A detailed experimental data base was created by measuring the frequency and SPL at various tube depths and spacing parameters for a range of NPR values (see Figs. 4 and 5). The resonance tube database consisted of measured frequencies at various depths. The frequency was measured for depths ranging from $d/D$ of 0.4 to 1.6 in steps of 0.2 $d/D$. From $d/D$ of 1.6 to 4.4 a depth increment of 0.4 $d/D$ was used. The spacing between the supply jet and the resonance tube was varied from $s/D$ of 0.4 to 2.8 in steps of 0.254 cm. The database covered a supply pressure range from NPR = 2.89 to 3.93 in 6 equal increments. Thus, we had 686 data points describing the behavior of the resonance tube at various depths, spacings

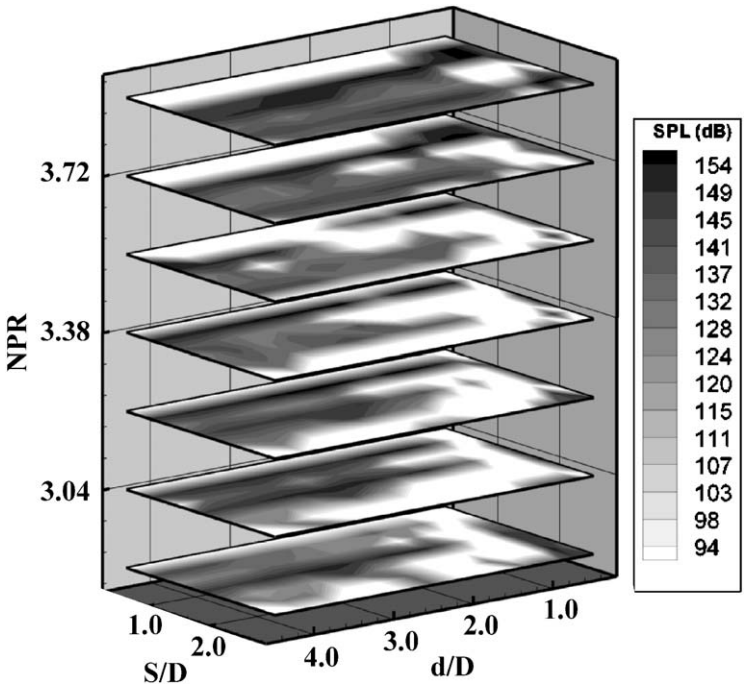


Fig. 4. Three-dimensional map of actuation SPLs for various values of the spacing parameter (jet-to-resonance tube), supply pressure and tube depth. (NPR_Standard = 1.15 NPR).

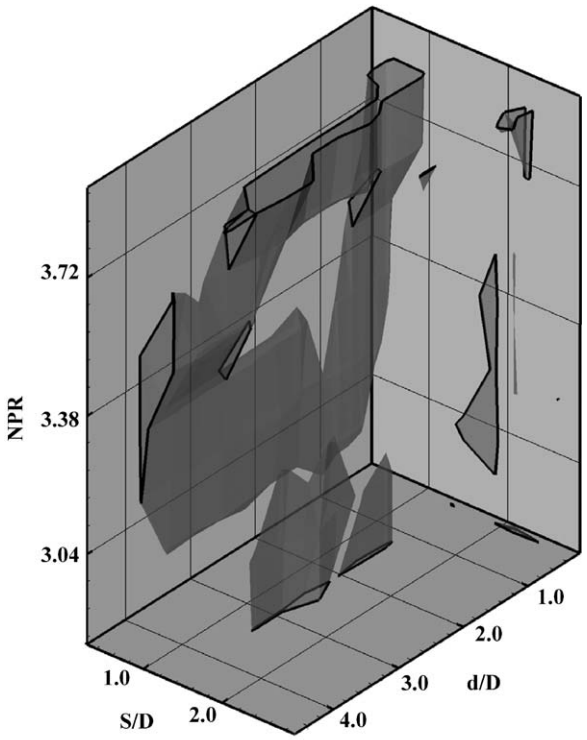


Fig. 5. Iso-surface extracted from three-dimensional map of Fig. 4. The 140 dB iso-surface represents the acceptable target amplitude for effective actuation. (NPR_Standard = 1.15 NPR).

and pressures. From Fig. 4 it is clear that on each plane there are limited regions of high amplitude. Thus an effective computer controlled actuator would have to search for the correct integration slot spacing at each depth.

The amplitude of actuation is characterized using metrics from linear acoustic theory such as acoustic power, $W$. This is derived from the SPL as follows: $\mathrm{SPL} = 20\log_{10}(p_{r.m.s.}/p_{ref})$ where $p_{ref} = 20\,\mu\mathrm{Pa}$. The acoustic power $W = (p^2_{r.m.s.}/c\rho_0)4\pi R^2$, where $R$ is the distance from the microphone to the resonance tube, $\rho_0$ is the density of air ($1.21\,\mathrm{kg/m^3}$), and $c$ is the ambient speed of sound (343 m/s). The metric described above is subject to several assumptions (including spherical radiation of sound into open space). The usefulness of the sound power metric is that it eliminates the microphone location as a parameter (SPL depends on the microphone location but the sound power is a characteristic of the source that is independent of microphone location). The acoustic efficiency of this device was calculated by taking the ratio of output power to input power. Input power is given by the product of supply pressure and volume flow rate. Output power was measured using a Kulite probe that was moved to the opening of the integration slot. At this location the Kulite sensor recorded a level of 169 dB. The acoustic efficiency was found to be 0.35% at 6.67 kHz if one considers the r.m.s. level integrated over the entire spectrum.

This database is then used to generate a look up table program for controlling the resonance tube such that the desired frequency is obtained at the highest amplitude. A Visual BASIC

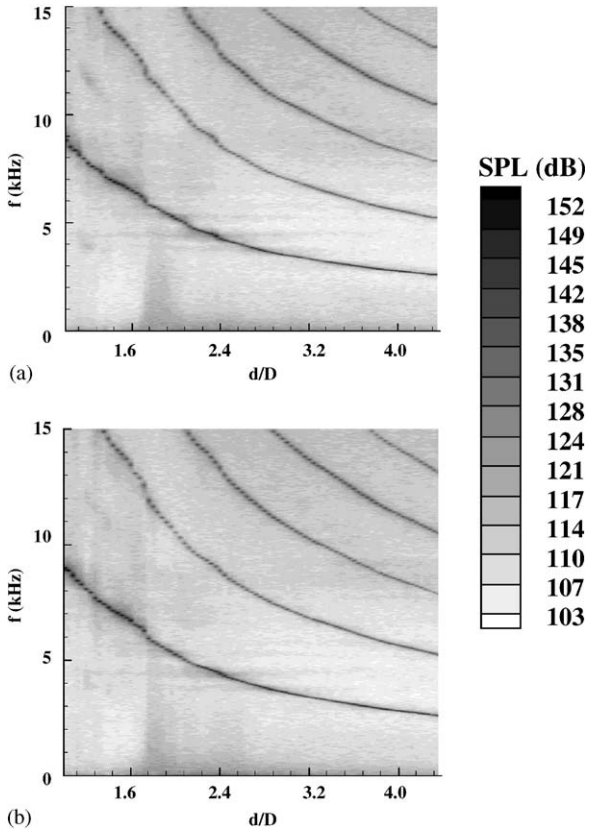


Fig. 6. Spectra at various resonance tube depths. (a) Decreasing depth, (b) increasing depth.

program was written in order to implement the look-up table database. The traversing mechanism was calibrated before generating the look up table program. When a desired frequency is input to the program it calculated the depth and moved the piston to the appropriate depth.

Figs. 6 and 7 depict the frequency variations when the tube depth is changed including the effect of hysteresis. The fundamental frequency (lowest curve) is tabulated and analyzed for errors in Tables 1 and 2.

### 3.2. *Pressure measurements within the PRT*

Flow visualization experiments conducted by Kastner and Samimy [22] have revealed some very interesting visual features of PRT actuators. However, a detailed characterization of unsteady pressures in the nearfield is desired and this is one of the objectives of the present work. Fig. 8 shows pressure time traces from sensors located internal and external to the tube. Measurements within and outside the tube were made at PRT operating frequencies of 2.5, 5 and 9 kHz. It should be mentioned that the time segment for the three parts is the same; 0.0011 s, which justifies the increase in number of cycles in each of part as the frequency increase. From Fig. 8 it can be seen that for all the frequencies, the shape of the pressure wave-form inside the

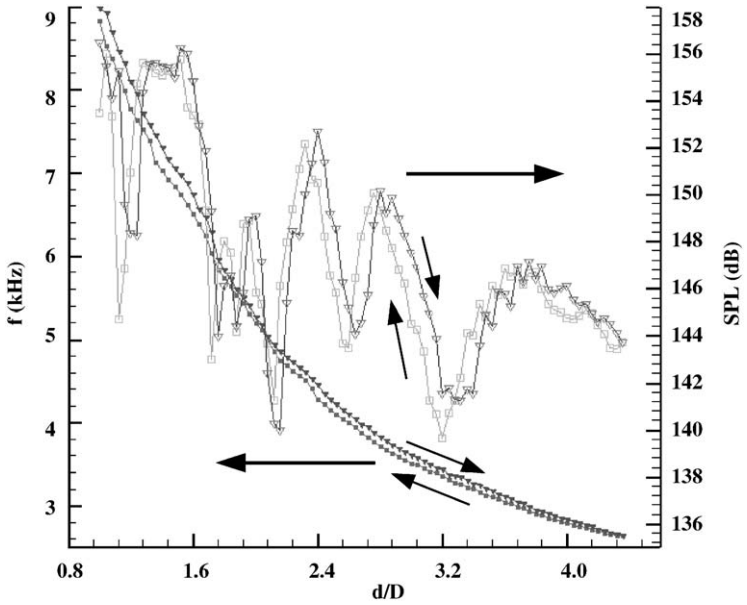


Fig. 7. Hysteresis errors in frequency and SPL with increasing and decreasing depth, where, —·— and —□— represent frequency and SPL, respectively for decreasing depth while —▼— and —▽— represent frequency and SPL, respectively for increasing depth.

tube was the same. For the 2.5 kHz case shown in Fig. 8(a) the pressure increases from −1000 Pa to 61,000 Pa in 56 μs (14% of cycle time), stays at 61,000 Pa for 216 μs (55% of cycle time) and decays back to −1000 Pa in 122 μs. (31% of cycle time) The total time is 394 μs after which the whole cycle repeats itself again. In the case of the 5 kHz tone shown in Fig. 8(b) the pressure rises from –13,000 to 61,000 Pa in 40 μs (19% of cycle time0, stays at 61,000 Pa for 102 μs (49% of cycle time) and then goes down to −13,000 Pa in 122 μs (32% of cycle time) with a total cycle time of 210 μs. Finally, for the 9 kHz case shown in Fig. 8(c) the pressure rises from –12,000 to 61,000 Pa in 34 μs (28% of cycle time), stays at 61,000 Pa for 42 μs (35% of cycle time) and then drops to −12,000 Pa in 45 μs (37% of cycle time) with a total cycle time of 210 μs. From the shape of the time series in all cases, it can be seen that the pressure time series inside the tube has a very regular shape. In contrast, the microphone signal is not very regular, possibly because of the reflections of sound in the near field by the traverse mechanism and supporting table.

The non-linear effects within the resonance tube are clearly illustrated by the results of Fig. 8. By examining the pressures within the tube it is found that in general, the dwell time is around 50% of the total cycle time and the rise time is less than the slew time. The rise time represents the time needed for the compression wave to travel in the tube and the slew time is the time needed for the expansion wave to travel out of the tube. By knowing these two facts, it is clear that the compression wave travels faster than the expansion wave.

The Quarter Wavelength Theory assumes that all the waves (compression, reflected compression, expansion and reflected expansion) are Mach waves and travel with the local speed of sound and the flow velocity in the tube is negligible. To examine this further the velocity of the compression and expansion waves for each case were calculated and are given in Table 6. It can be

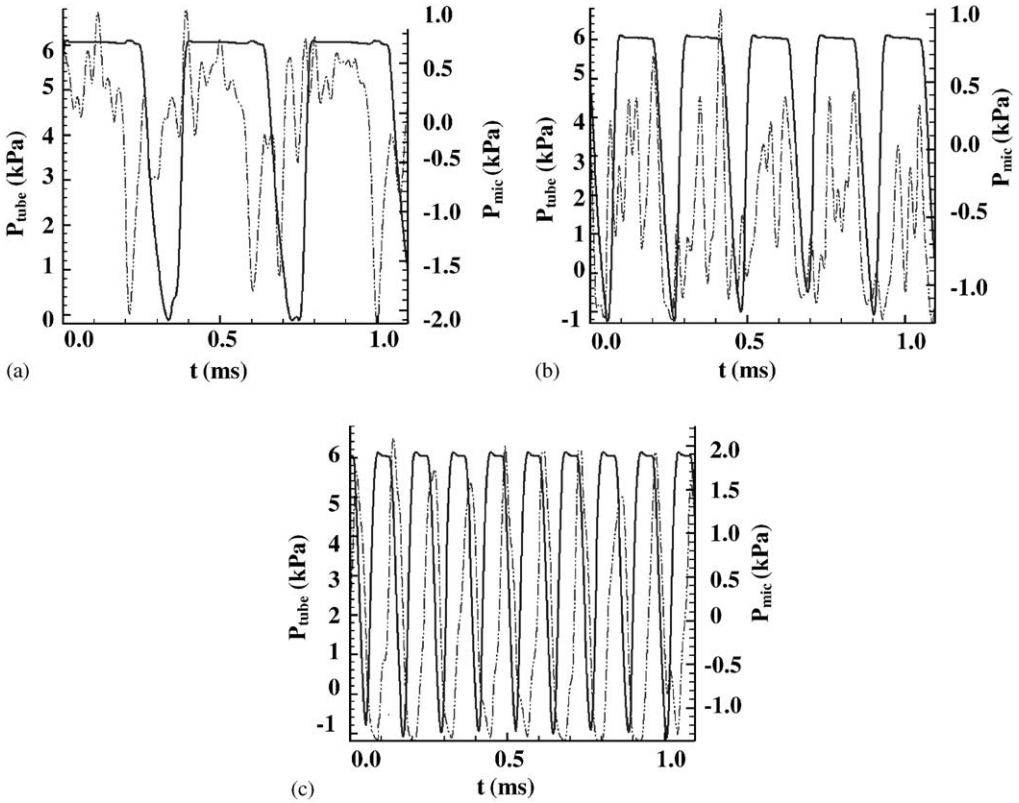


Fig. 8. Pressure time series from externally located microphone (–· ·–· ·–) and from pressure transducer at the closed end of the tube (——) at various frequencies. (a) 2.5 kHz, (b) 5 kHz, (c) 9 kHz.

seen that the velocity of the compression wave is higher than that of the expansion wave and as the frequency increases (depth decreases) the velocity decreases for both compression and expansion waves. In addition, the compression wave velocity is higher than the speed of sound. At 9 kHz the calculated velocities for both compression and expansion waves are less than the speed of sound. The time trace measured within the tube displays a longer dwell time at high pressures alternating with shorter dwell times at low pressures. In contrast, for the time trace measured outside the tube the dwell times are indistinguishable.

### 3.3. Detailed characterization of the near field

The nearfield data shown in Figs. 9 and 10 represent the $YZ$ and $XY$ planes I and II (see Fig. 2). The data for planes I and II were obtained by traversing a Kulite sensor over the entire near field. Part (a) of Figs. 9 and 10 shows the total r.m.s. pressure signal integrated over the entire spectrum. Part (b) represents the pressure levels at the actuation frequency and (c) represents the phase relative to a second fixed sensor. Note that the propagation of the wave is normal to the phase front.

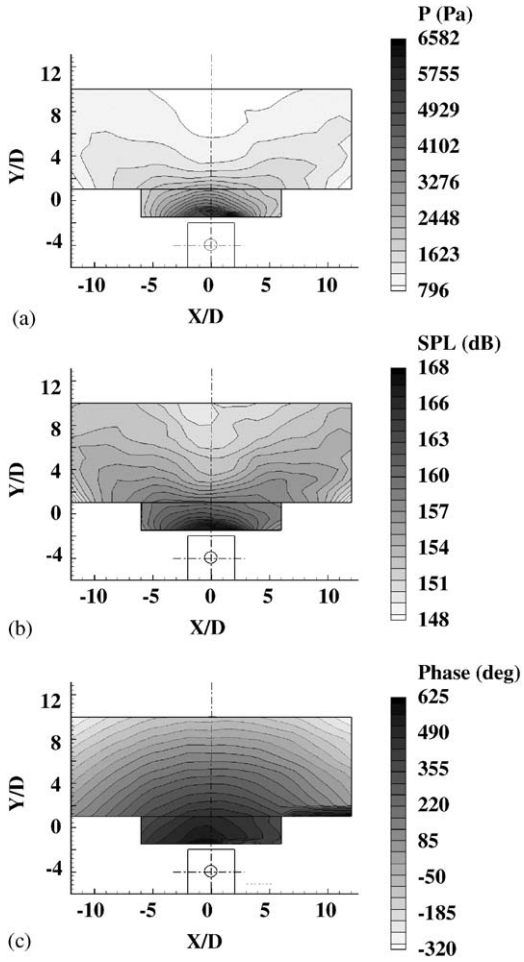


Fig. 9. Time-averaged features in the near field on the $XY$ plane (I and II). (a) RMS pressure levels, (b) SPLs at actuation frequency, (c) relative phase (degrees). NPR (NPR_Standard = 1.15 NPR) = 3.38, $s/D = 1$ and $d/D = 1$.

The data shown in Figs. 9 and 10 reveal some very interesting features. In the transverse plane ($XY$, Fig. 9) the actuation signal exhibits two distinct lobes caused perhaps by a transverse flapping mode instability (this flapping instability appears to prefer the transverse direction over the vertical direction where the jet is constrained at the bottom). The phase data exhibit isotropy. Fig. 10 represents data in the axial plane ($YZ$) and shows that the actuation is biased at 9 kHz in the upstream direction (relative to the direction of the supply jet). This finding is significant and may determine the deployment configuration of the actuator. For example, with the free stream going from left to right, one may want to have the actuation opposing the free stream in a counterflow like fashion for jet mixing enhancement applications or alternatively choose a coflowing arrangement as in directed synthetic jets. The directivity of the PRT on the $YZ$ plane is shown in Fig. 11. Detailed phase averaged data are shown in Figs. 12 and 13 for the $XY$ and $YZ$

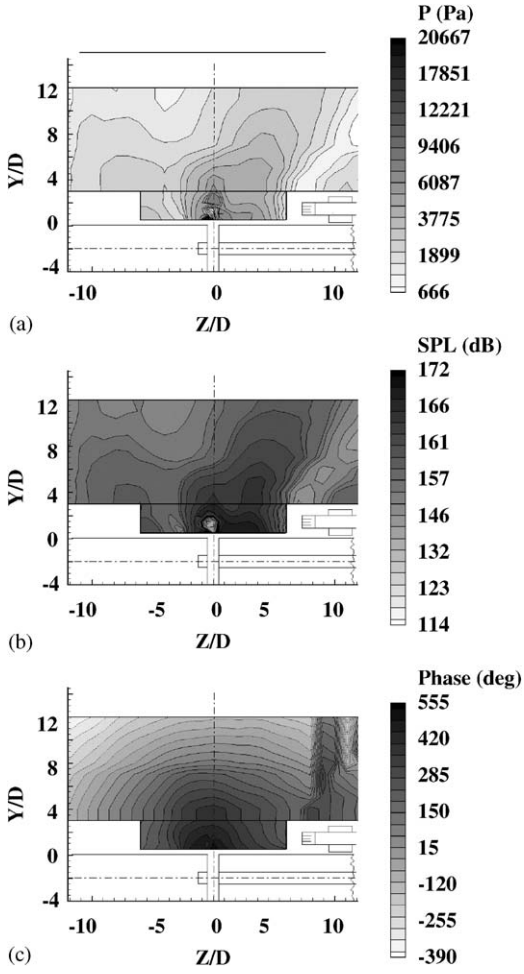


Fig. 10. Time-averaged features in the near field on the *YZ* plane (I and II). (a) RMS pressure levels, (b) SPLs at actuation frequency, (c) relative phase (degrees). Compressed air flow in actuator is from right to left. NPR (NPR_Standard = 1.15 NPR) = 3.38, $s/D = 1$ and $d/D = 1$.

planes (I, II). The measurements were made by moving a sensor over the entire nearfield (see measurement grid in each figure) and using a second reference sensor as a trigger for phase-averaging. Phase averaged data were acquired at an operating NPR of 3.5, $s/D = 1$ spacing and an operational frequency of 9 kHz ($d/D \approx 0.92$) with a sampling frequency of 200 kHz. The reference microphone was band pass filtered (between 8 and 10 kHz) and the probe signal was analog low pass filtered at 16 kHz prior to sampling; its purpose is to remove high-frequency components that would otherwise be aliased, or folded down to lower frequencies. Data were ensemble averaged over 100 oscillation cycles. The phase difference from frame-to-frame is 36°. By comparing the phase averaged information of Fig. 12 to the time averaged picture of Fig. 9 one can see how the dual lobes emerge on averaging over time.

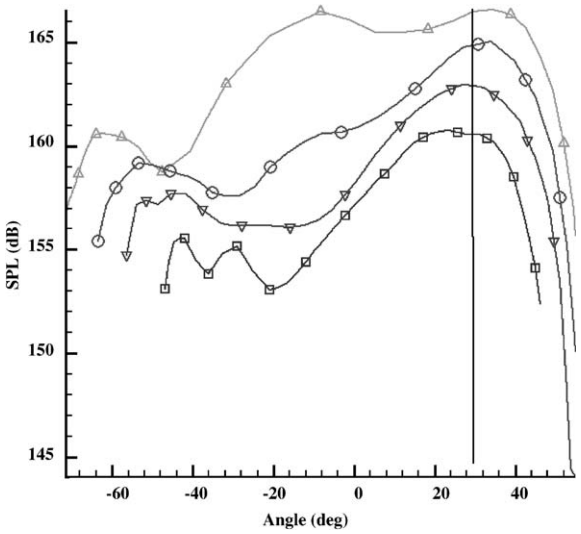


Fig. 11. Sound pressure directivity of the PRT in the $YZ$ plane. Angles are with respect to the $Y$-axis. —△—, $Y/D = 4$; —○—, $Y/D = 6$; —▽—, $Y/D = 8$; and —□—, $Y/D = 11$.

### 3.4. Simulation studies

In this section we discuss the simulation of PRT actuator flow fields. The formulation of the computational problem and numerical methods are summarized followed by a discussion of key results and physical insights.

To explore the flow physics and better understand mechanisms, direct numerical simulations of the resonance tube's flow field were performed using the WIND flow solver. WIND is a general purpose Euler and Navier–Stokes Solver. The simulations provide details of the unsteady flow inside the actuator, as well as features of external acoustic radiation. Final solutions were obtained using the WIND code with a third order spatial scheme and third order Runge–Kutta time integration. Although the work of Cain and Bower [23] suggests the use of a fifth order scheme, the presence of internal zone boundaries makes the third order scheme advantageous in this application. The choice of the third order spatial scheme was dictated by the presence of numerically transparent zone boundaries in the present work. To minimize the issue of outer boundary reflections "buffer zones" were used with numerical damping in these buffer regions only. Grid refinement and algorithm studies suggest that the present results are invariant to grid and algorithm for modest changes.

The geometry fabricated in the laboratory had a number of complexities that would require an unreasonably large grid and enormous computational resources to simulate. In order to do meaningful simulations with reasonable computational resource requirements, simplifying approximations are required. The first such approximation is to assume an axisymmetric geometry and flow field. The second approximation is a reduced Reynolds number that permits direct numerical simulations with a modest grid.

The basic geometry for the computation consists of a supply tube feeding the integration slot and resonance tube, and an axisymmetric far field. The supply tube has a 1.27 cm diameter at the

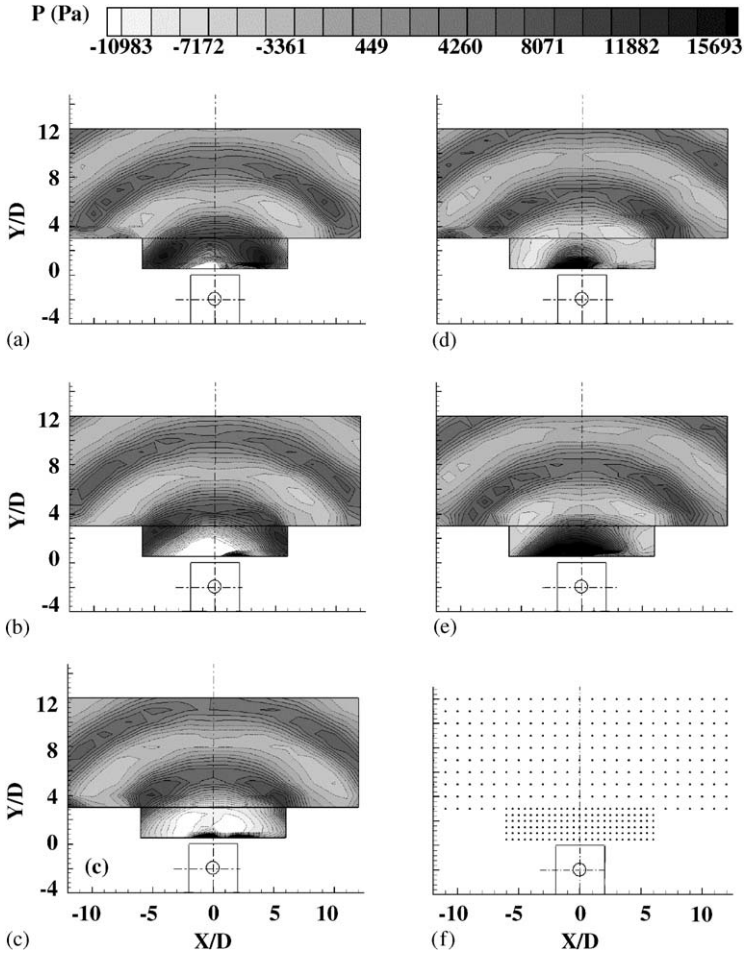


Fig. 12. Phase-averaged near field pressure depicted on the $XY$ plane (I and II). Phase difference from frame-to-frame (a–e) is 72°. Measurement grid is shown in (f).

reservoir, tapers conically to a 0.635 cm diameter constant section, and then has a brief flare into the integration slot. The conical section and the constant diameter section are both 1.27 cm long. The grid in the supply tube, integration slot, and resonance tube has nominally square cells roughly 0.01575 cm on a side. In the far field the cell size gradually expands from 0.01575 cm to roughly 0.254 cm on a side. Thus, there are roughly 280 cells per acoustic wavelength in the supply tube, integration slot and resonance tube, and at least 16 cells per wavelength at the far edges of the outer grid.

A typical sound radiation field, characterized by the far field, is shown in Fig. 14. The simulation shown in Fig. 14 is based on viscous no-slip boundary conditions, which will be shown to be quite important. The fields in Fig. 14(a,b) are snapshots spanning approximately one period of oscillation, after the calculation has advanced 31,400 timesteps. At this point in the calculation the field has advanced approximately 16 periods of the basic 7.6 kHz resonance. In the first wavelength (approximately 4.445 cm) from the integration slot, some asymmetries are present. As

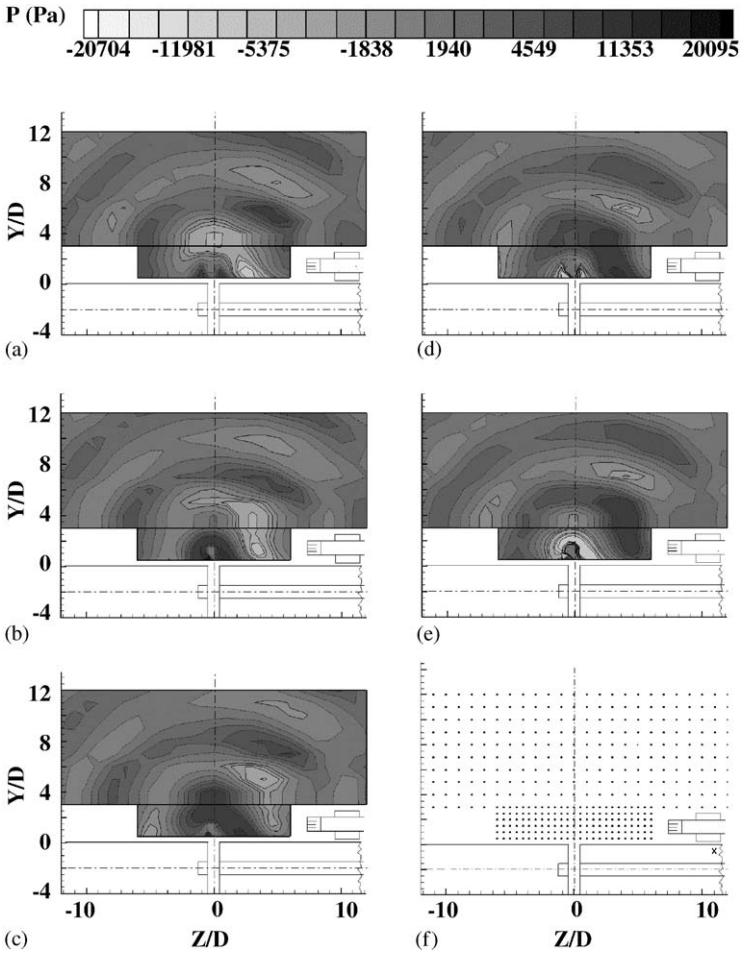


Fig. 13. Phase-averaged near field pressure depicted on the *YZ* plane (I and II). Phase difference from frame-to-frame (a–e) is 72°. Measurement grid is shown in (f). Compressed air flow in actuator is from right to left.

the pressure wave moves into the far field, the evolution shows stronger radiation to the left than to the right. One possible explanation is that the asymmetric flow in the integration slot turns the acoustic waves to the left.

A more detailed perspective of the source field is given by the corresponding Mach contours in the supply tube, integration slot, and resonance tube, shown in Fig. 15(a–c). There are two major points from Fig. 15(a–c). First note that the flow in the integration slot is almost entirely confined to a narrow channel up the wall on the resonance tube side. This feature is present in all snapshots examined. The second important point is that the shock structure oscillates back and forth across the integration slot, varying in extent from as far as $\frac{7}{8}$ of the distance across the integration slot to as little as $\frac{1}{4}$ of the distance across the integration slot.

An alternative problem formulation using slip wall boundary conditions was executed to gain further insight into the physics of this problem. From these alternate formulation results, we speculate that the unsteady chamfer (recall the presence of a chamfer at the end of the supply

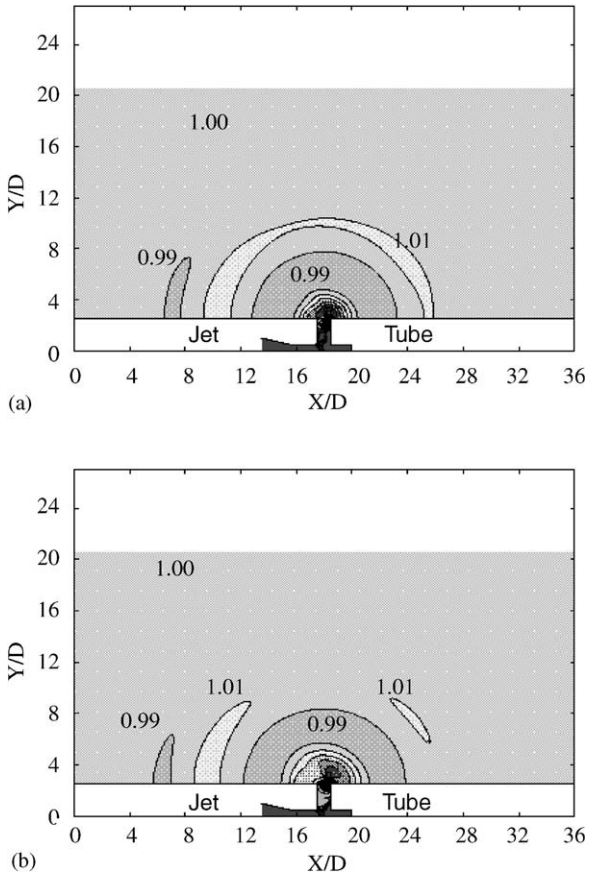


Fig. 14. Pressure contours from a simulation of a PRT using the WIND code with buffer zones to minimize reflected pressure waves from the outer boundaries. The nozzle pressure ratio for these simulations was 3.72. Timesteps: (a) 32,400 and (b) 32,600. Compressed air flow in actuator is from left to right.

nozzle) separation is driven by the acoustic resonance, and that the unsteady separation in turn drives the unsteady shock system thereby closing the loop. It was found that the location of the separation point on the chamfer oscillates significantly during the resonance cycle; the separation on the chamfer can occur as early as $\frac{1}{4}$ of the chamfer distance or remain attached to the end of the chamfer.

The periodic nature of the flow and acoustic field is illustrated by a pressure measurement, taken at the bottom of zone 4 about 0.635 cm from the edge of the integration slot. Fig. 16 shows the time history of the pressure and its basic periodic nature over the first 30,000 timesteps of evolution of a slip wall calculation. Comparison of these slip and no-slip cases suggests that the flow separation of the supply jet is very important.

One additional difference between the computations and experiments concerns details of the geometry. The computational supply jet issues from a smooth contraction as previously described. In contrast, the experimental geometry contains a sudden contraction. Losses for a sudden contraction in incompressible flow are approximately 35% based on the information in Blevins

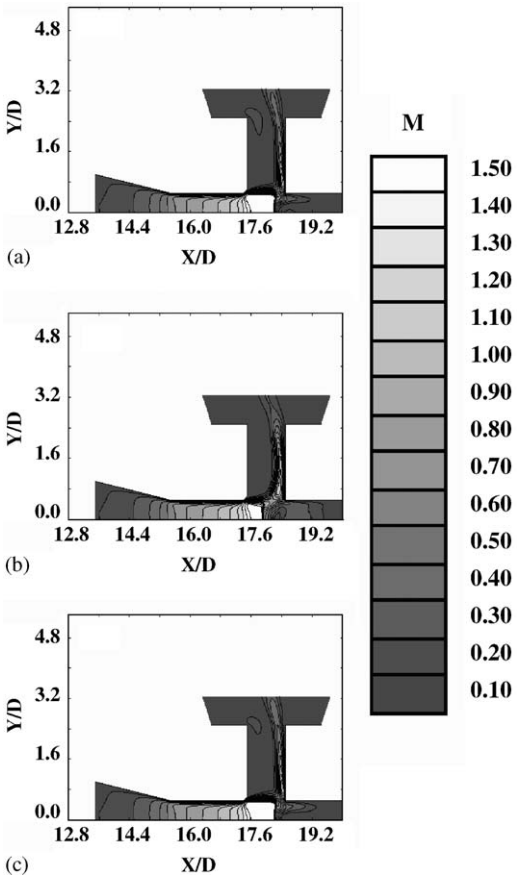


Fig. 15. Iso-Mach contours from a simulation of a PRT using the WIND code. The nozzle pressure ratio for these simulations was 3.72. Timesteps: (a) 31,400, (b) 32,200 and (c) 33,200. Compressed air flow in actuator is from left to right.

[24]. The computational frequency response discussed below suggests that the experiments have a 24% system loss. The direct experimentally measured loss was 28.4%.

### 3.5. *Approaches for controlling the PRT*

The two approaches to devising a high-bandwidth PRT are depicted in Fig. 17. The first approach was a LUT approach that relied on an extensive database. The second approach used either the quarter wave length (QWL) or the LUT as an initial estimate and varied either the resonance tube depth, $d$ (SISO) or both the spacing parameter, $sp$ and the depth, $d$ (MIMO) within a feedback loop until satisfactory results were obtained.

Based on the extensive database, it was found that the resonance tube depth is the primary parameter in controlling the PRT's resonance frequency. In addition we found that if the correct values of pressure and spacing were used, changing only the depth can produce frequencies ranging from 2700 to 9000 Hz. For the computer controlled PRT tests we chose an NPR of 3.5

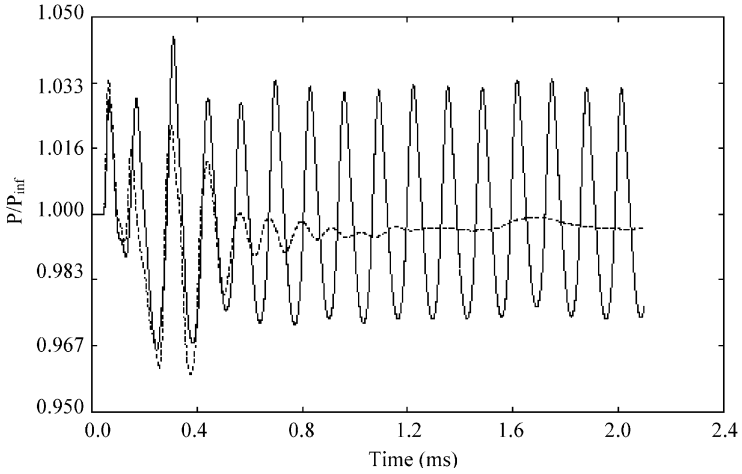


Fig. 16. A time trace of the pressure in the far field with the solid line (——) corresponding to the case that produced the snapshots shown in Figs. 14 and 15 and the dashed line (- - - - -) corresponding to a slip wall calculation. Solution calculated for 30,000 timesteps.

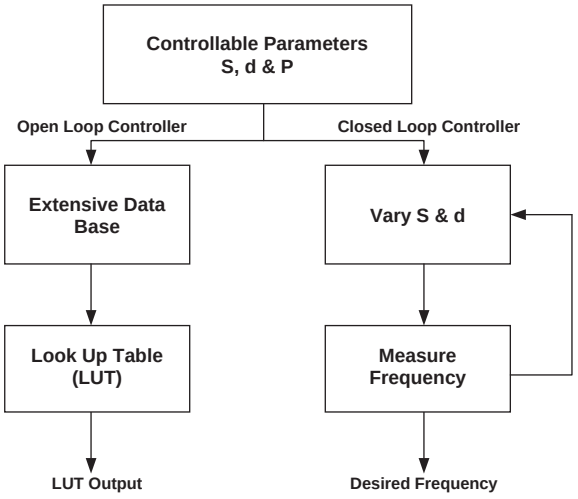


Fig. 17. Two approaches to creating a computer controlled high-bandwidth actuator.

and a spacing of $s/D = 1$ were chosen based on the results of Fig. 4. Then, after averaging both increasing and decreasing depth curves, a 6th order polynomial curve fit to the data was obtained. The equation representing the curve fit is:

$$d/D = 11.6168 \times 10 - 24f^6 - 7.0172 \times 10^{-19}f^5 + 20.2436 \times 10^{-15}f^4 - 29.782 \times 10^{-11}f^3 + 22.9436 \times 10^{-7}f^2 - 9.1516 \times 10^{-3}f + 16.9996,$$

where $f$ is the required frequency (Hz), $d/D$ the depth ratio.

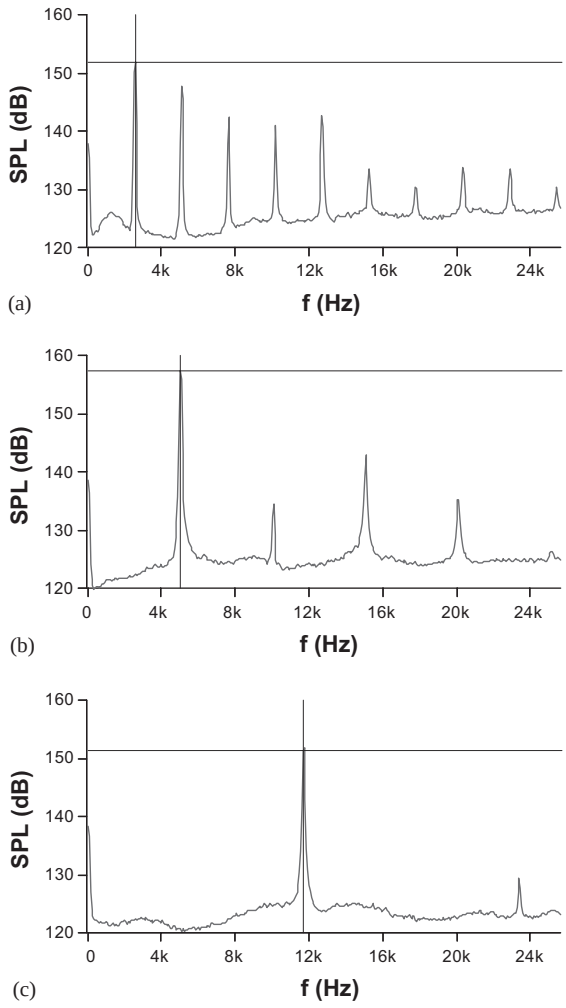


Fig. 18. Spectra showing results of the LUT approach. The vertical line depicts the prescribed frequency and the spectrum represents the resulting actuation signal (see Table 1 for the errors in using this method). (a) $d/D = 4$, input and output frequencies are 2.50 and 2.56 kHz, respectively, (b) $d/D = 2$, input and output frequencies are 5.00 and 4.99 kHz, respectively and (c) $d/D = 0.4$, input and output frequencies are 11.00 and 11.65 kHz, respectively. NPR = 3.72 (NPR_Standard = 1.15 NPR).

Some of the results of this type of controller are shown in Fig. 18 in the form of spectra of the sound produced. In addition Table 3 provides information on the input frequency, output frequency and the output frequency error. From these results it can be seen that this method produced the prescribed frequency with a maximum error of 6%. But in addition to the errors shown in the table, changes in supply pressure could create situations where the device produced no tones at a given integration slot spacing. In addition if errors occurred in the plant (or the system) or if noise was present, the controller could not respond since it did not receive any feedback. It is therefore necessary to search for a more robust method that incorporates feedback to handle noise within the system and reduce the output error.

Table 3
Summary of effectiveness of look up table (LUT) approach and feedback controller (FB) in producing high-frequency excitation signals based on prescribed inputs in ascending order. The error when using the feedback controller depends on the frequency bandwidth (20 Hz for our experiments) that depends on sampling frequency (80 kHz) and number of points in the spectrum (4096)

| Input frequency (kHz) | LUT output frequency (kHz) | LUT %error | FB output frequency | FB %error |
|---|---|---|---|---|
| 2.5 | 2.56 | 2.40 | 2.52 | 0.80 |
| 3 | 3.008 | 0.27 | 2.99 | 0.67 |
| 4 | 4.023 | 0.57 | 4.02 | 0.50 |
| 5 | 4.992 | 0.16 | 5.02 | 0.40 |
| 6 | 6.144 | 2.40 | 6.01 | 0.20 |
| 7 | 6.976 | 0.34 | 7.02 | 0.29 |
| 8 | 8.046 | 0.57 | 8.02 | 0.25 |
| 9 | 9.216 | 2.40 | 8.98 | 0.22 |
| 10 | 10.3 | 3.00 | 9.99 | 0.01 |
| 11 | 11.65 | 5.91 | 10.98 | 0.18 |

Table 4
Effect of resonance tube depth ratio ($d/D$) on the resulting frequency, sound pressure level, acoustic power and acoustic energy (spacing parameter, $s/D = 1.2$, NPR = 3.72)

| $d/D$ | $f$ (kHz) | SPL (dB) | $P_{r.m.s.}$ (Pa) | $W$ (W) | $E$ (J) | Eff % |
|---|---|---|---|---|---|---|
| 0.4 | 11.58 | 137 | 141.59 | 0.18 | 0.15 | 0.003 |
| 0.6 | 10.75 | 154 | 1002.37 | 8.89 | 7.37 | 0.175 |
| 0.8 | 9.41 | 156 | 1261.91 | 14.10 | 11.83 | 0.278 |
| 1.0 | 8.32 | 155 | 1124.68 | 11.20 | 9.54 | 0.221 |
| 1.2 | 7.36 | 151 | 709.63 | 4.46 | 3.87 | 0.088 |
| 1.4 | 6.66 | 157 | 1415.89 | 17.74 | 15.70 | 0.350 |
| 1.6 | 6.14 | 156 | 1261.91 | 14.10 | 12.70 | 0.278 |
| 2.0 | 5.25 | 154 | 1002.37 | 8.89 | 8.36 | 0.175 |
| 2.4 | 4.10 | 154 | 1002.37 | 8.89 | 9.20 | 0.175 |
| 2.8 | 3.46 | 154 | 1002.37 | 8.89 | 10.07 | 0.175 |
| 3.2 | 3.07 | 152 | 796.21 | 5.61 | 6.86 | 0.111 |
| 3.6 | 2.75 | 152 | 796.21 | 5.61 | 7.45 | 0.111 |
| 4.0 | 2.56 | 149 | 563.68 | 2.81 | 3.97 | 0.055 |
| 4.4 | 2.37 | 150 | 632.46 | 3.54 | 5.36 | 0.070 |

The effectiveness of the LUT and FB approaches is summarized in Tables 3 and 4. Note that ($f_{target}$) is the target (input) frequency, ($e\%$) is the percentage error and the data given in the table is the resulting frequency. The look up table method was made possible by very detailed data taken under various conditions. Details of the resonance tube depth on the resulting frequency, SPL, and acoustic power are given in Tables 4, 5. Significant improvement is obtained by using feedback. Fig. 19 compares various control strategies in obtaining the prescribed frequency. The departure from the QWL prediction increases at higher frequencies (lower tube depths). If the QWL is used as an initial estimator reasonable convergence is obtained within 8 iterations. If one

Table 5
Time analysis of pressure time series inside the tube

| Case | $t$ rise (μs) | Rise % | $t$-dwell (μs) | Dwell % | $t$-slew (μs) | Slew % | $t$-total (μs) |
|---|---|---|---|---|---|---|---|
| 2.5 kHz | 56 | 14 | 216 | 55 | 122 | 31 | 394 |
| 5 kHz | 40 | 19 | 102 | 49 | 68 | 32 | 210 |
| 9 kHz | 34 | 28 | 42 | 35 | 45 | 37 | 121 |

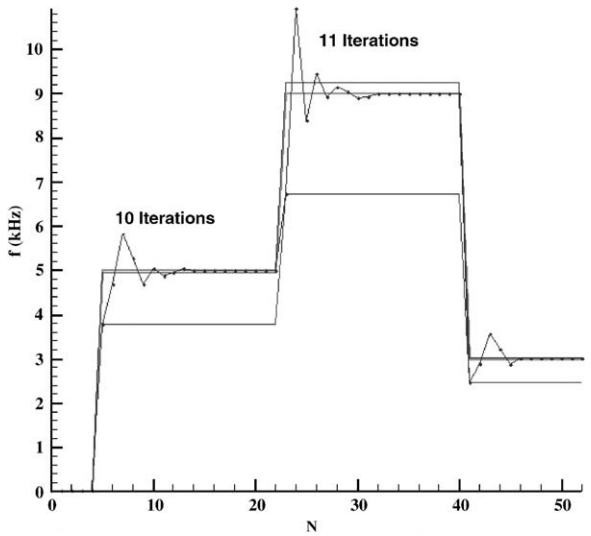


Fig. 19. Effectiveness of various control strategies in obtaining a prescribed frequency. The comparison includes the input frequency (——), quarter wavelength estimation (QWL) (— — —), look up table method (LUT) (— — —) and single input single output (SISO) feedback controller (FB) (using look up table method as initial estimator) (— · —).

uses the LUT as an initial estimator the SISO controller provides better results (Fig. 20). Due to the complexity of the functioning of the PRT, SISO control is not very effective. Five possible problems are illustrated in Fig. 21.

The first step towards building a closed loop controller was to make it a single input (frequency) single output (depth) (SISO). In this step, we started by using the QWL theory as an estimator and a routine needed to be chosen for iterating depth ($d$). A fixed-point iteration method was used to iterate for the depth and this produced the prescribed frequency. A depth increment of $d/D = 0.2$ was used for the results presented in this paper. The iteration was limited by the error between the measured frequency and the input frequency. And this error was calculated based on the input parameters for the spectral calculations such as, sampling frequency and number of points per record, which defined the resolution of the spectrum calculated. This controller was built using a LABVIEW program that acquired the data from the microphone, calculated the spectrum, and iteratively changed depth. Fig. 19 shows the differences in errors resulting from the use of the QWL as an open loop controller, using the LUT as an open loop controller and the feedback

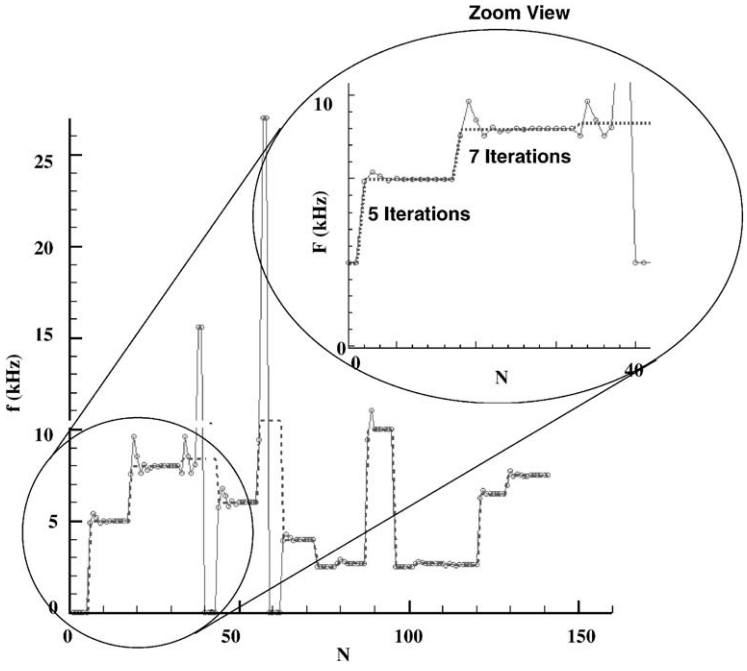


Fig. 20. Effectiveness of single input single output (SISO) feedback controller (FB) (—○—) showing its response to various input frequencies (-------) using the LUT as an initial estimator.

controller (FB), which uses the QWL as an initial estimator. It can be seen that the feedback controller reduced the error to around 20 Hz (based on 4096 point per record and 80 kHz sampling rate), which in comparison to both QWL and LUT is a huge step in improving the control. It should be mentioned that the iteration time depends on the time required to acquire the data, the time required to calculate the spectrum and the time required to move the motor to the new depth. In order to reduce the time required to lock on to a frequency one can either reduce the iteration time or the number of iterations. To reduce the iteration time, the time needed to acquire the data to calculate the spectrum can be reduced by increasing the sampling rate, reducing the number of points per record, or reducing the number of records, or increasing the speed of the motor. To reduce the number of iterations, the LUT was proposed as an estimator based on the results shown in Fig. 19. Fig. 20 shows the results and response of such a controller. This controller could successfully reduce the number of iterations to 30% of that required when the QWL was used as an estimator, for the same value of error tolerance (as seen on the zoomed view). In general, it can be seen that the controller works well and finds the prescribed frequency within 3–8 iterations. However, there are some situations where the controller failed to work. For example, when the prescribed frequency was 8.2 kHz, the controller failed since a harmonic appeared at 16 kHz. This result and others created some challenges for the user. These challenges are summarized in Fig. 21.

Fig. 21(a) shows the spectrum vs. depth contours under favorable conditions of spacing and pressure, which are not easy to obtain at all times. For example, (Fig. 21b and f) show how the

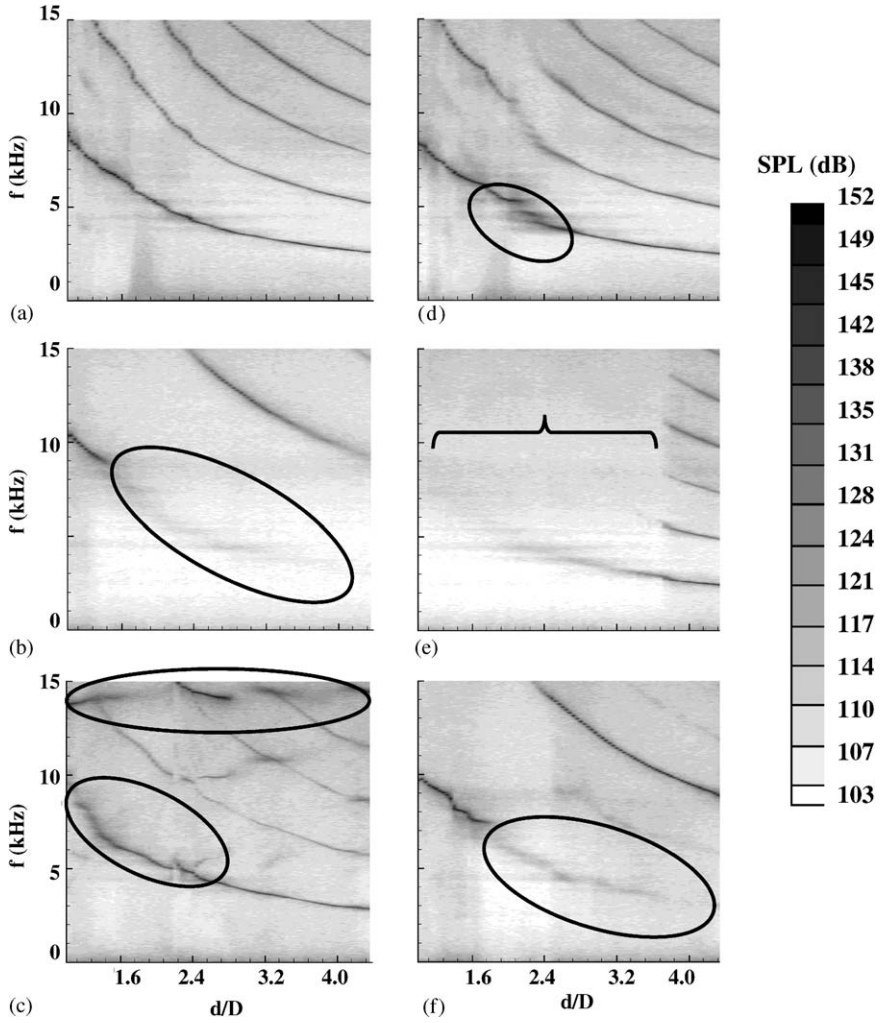


Fig. 21. Features of the PRT that make the LUT approach ineffective (see marked regions). Pressure spectra with changing depth are shown for the following cases. (a) Optimal case, (b) jump to higher harmonics, (c) high-frequency noise, (d) frequency gaps, (e) only low frequency, (f) higher harmonic jumps with frequency gaps.

higher harmonics can dominate the spectrum, and makes it impossible to obtain a frequency lower than 8.5 kHz. Fig. 21(c) shows the presence of high-frequency noise at different depths, which makes it difficult for the controller to find the required frequency. In some cases the frequency variation was not continuous i.e., some gaps appeared at specific frequencies, which make it difficult for the controller to find certain frequencies as shown in Fig. 21(c) and (d). In other cases only low frequencies can be found in the spectrum and no tones appeared at depths where high frequencies were expected, as shown in Fig. 21(e). In order to solve these problems, a second input to the controller was required. Since the integration slot spacing acts like a tuning parameter, it could be varied to change the shape of the contours (shown in Fig. 21) and at the same time change the SPL, i.e., to obtain maximum SPL at a given frequency.

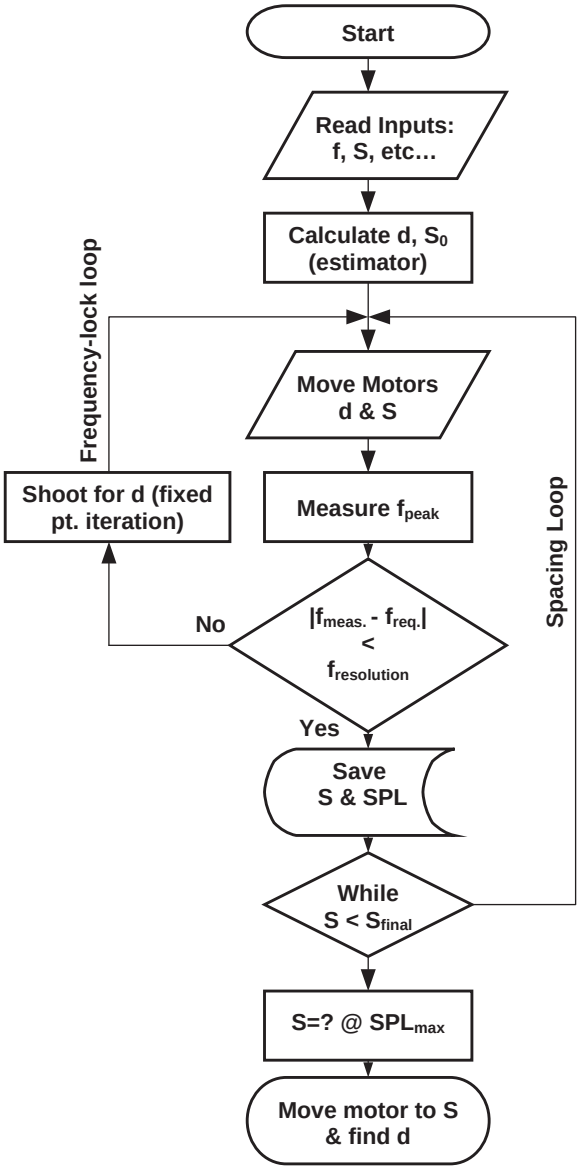


Fig. 22. Flow chart of the algorithm for the multi input multi output (MIMO) feedback controller (FB) used to control both the spacing and the depth of the PRT.

In the improved approach the spacing parameter was scanned to find the best value (one that produced the maximum SPL). The spacing is limited to a specific range, which is the instability region of the diamond shape shock cell structure of the jet. So, the minimum, maximum and step size of the spacing were fed into the controller. Following this, each spacing step was applied, the frequency was locked on to using the program used previously (frequency lock loop), the SPL was saved and a new step was initiated (the spacing loop) as shown in the flow chart of Fig. 22. When the spacing loop yielded the maximum possible value of SPL, the spacing corresponding to the

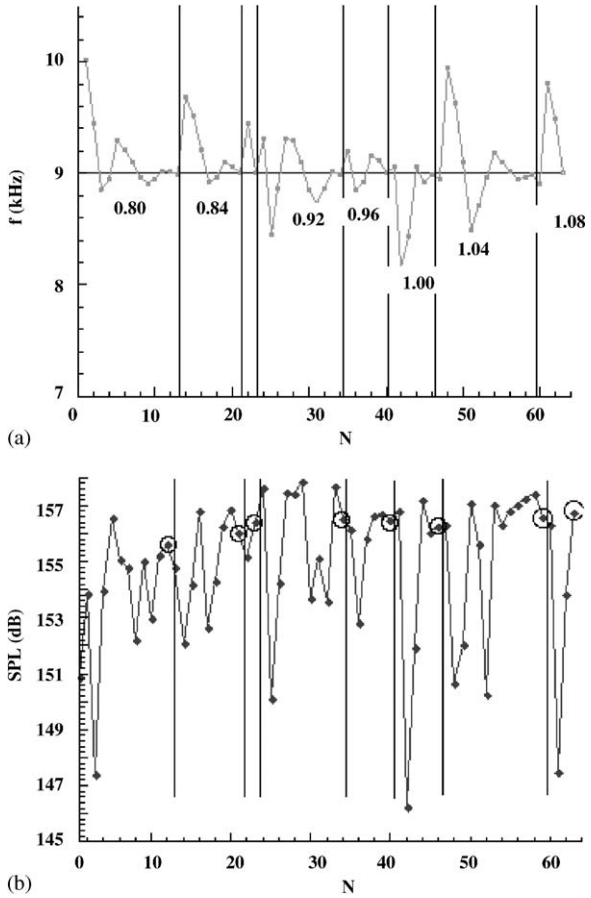


Fig. 23. Response of the MIMO feedback controller (—■—) for an input frequency of 9 kHz (———). The figure also illustrates the scanning of the spacing parameter ($S/D$) from 0.8 to 1.08 to produce the prescribed frequency at the highest amplitude. (—⊛—) Represents the saved points. (a) Frequency and (b) SPL.

maximum value of SPL, was chosen and the frequency-lock program was run again. The response of this controller for an input frequency of 9 kHz and spacing range of $s/D = 0.8-1.08$ with a 0.254 cm step size is represented in Fig. 23. The plot shows 8 fields, starting from $s/D = 0.8$ to 1.08, which represents the spacing used each time in the spacing loop. The prescribed and measured frequencies vs. number of iterations are plotted in the upper part and SPL vs. number of iteration are plotted in the lower part. So, for example at a spacing of $s/D = 0.8$ the frequency was locked at 9 kHz after 13 iterations and the corresponding SPL (155 dB) was saved. Then, the next spacing was set ($s/D = 0.84$) and the same procedure repeated (Table 6).

The stored data points of the spacing and SPL are marked in circles. Based on these results, the optimal spacing of $s/D = 1.08$, which produced the maximum SPL, was chosen and the frequency lock routine was run again, to obtain 9 kHz at 157 dB. It should be mentioned here that logic was incorporated into the program to terminate the frequency-lock loop if any unusual result occurs (like higher harmonics, frequency gaps… etc).

Table 6
The calculated velocities of the compression and expansion waves

| Case | *t*-rise (μs) | Velocity (ft/s) | Mach no. | *t*-slew (μs) | Velocity (ft/s) | Mach no. |
|---|---|---|---|---|---|---|
| 2.5 kHz | 56 | 1785.71 | 1.64835 | 122 | 819.672 | 0.75662 |
| 5 kHz | 40 | 1041.67 | 0.96154 | 68 | 612.745 | 0.56561 |
| 9 kHz | 34 | 612.745 | 0.56561 | 45 | 462.963 | 0.42735 |

Since the PRT phenomenon is non-linear and it is hard to predict the occurrence of the tone, a fixed-point iteration method was used as a controller. By examining this type of method, it can be easily noticed that it is a pure gain change method. The time needed by this controller to lock to the required frequency was presented in the current study as number of iterations. The time needed for each single iteration mainly depends on the time needed to collect the points and on the time of moving the motors to the required distance.

When using the SISO FB controller, it was found that it can compensate for internal noise, and sometimes for external noise as well. But, for some cases, it could not compensate for large external perturbations such as a big change in pressure. As a result the MIMO FB controller was constructed. From the mapping results, it was found that the pressure and spacing are correlated. So, if the pressure changes and results in the absence of resonance, a change in spacing can compensate for that and can produce the resonance again. Based on this observation, the MIMO FB controller was built. Where it scans a range of spacing specified by the user locks on to the required frequency, and saves the corresponding SPL value at each spacing value. So, using this controller we did not only solve the problem in producing the tone if the pressure condition changed, but we also could make it find the highest SPL level at that frequency. To demonstrate the improvements obtained using this closed loop controller over the open loop type, various frequencies where chosen to be run on both controllers and the resultant frequency is tabulated in Table 4. The table shows a significant reduction in error when going from the LUT method to the FB method. Where in LUT method the maximum error was 5.9% compared to 0.8% in FB method. The last point to be discussed about the controller is the role of the estimator; it was clearly shown how the estimator affects the number of iterations needed by the controller to lock on to the required frequency. It was shown that the LUT estimator reduced the number of iterations by 30% compared to the QWL estimator. Since the LUT estimator was based on a 6th degree polynomial curve fit, an increase in the degree or in the significant figures in the fitting equation can result in more accurate estimator, and consequently less iteration and faster control.

## 4. Concluding remarks

We developed and demonstrated a high-bandwidth actuator based on the PRT concept. The PRT concept involves a high-speed jet that impinges on the open end of an open–closed resonance tube. This device is capable of producing flow oscillations of high amplitude and high frequency. The actuator could produce frequencies ranging from 500 to 15,000 Hz at amplitudes up to 160 dB. The experimental developments were complemented by analytical modelling and direct numerical simulations.

Analytical modelling of the acoustic resonances in the PRT geometry [22] was carried out in order to understand how the geometrical parameters influence the resonance frequency. For the smaller tube depths, associated with higher resonance frequencies, the integration slot geometry was found to play an important role in determining the resonant frequency. Direct numerical simulations of the unsteady flow in the PRT actuator were carried out in order to explore the flow physics and better understand the fundamental mechanisms responsible for the resonance. Scaled simulations of the powered resonance have been achieved with good correspondence to laboratory experiments in terms of the frequency (simulated at 7.6 kHz) and amplitude (a simulation value of 160 dB) of their resonant response. The simulations suggest new insights into the complexity and details of the flow field.

The simulations show that the flow in the integration slot is primarily on the resonance tube side with almost no flow on the supply tube side of the integration slot. The numerical results suggest that the acoustic waves from resonance in the resonance tube drive an unsteady separation at the supply tube. The unsteady separation at the supply tube in turn drives the observed large oscillations in the shock structure. The unsteady separation seems to be a key aspect of the resonance phenomena. Extensive experimental data were acquired and then used to create a look up table program for computer controlled operation. Detailed measurements useful for understanding physics and validating simulations were made. The detailed characterization also provides guidance for actuator deployment. Finally, we have grounds to believe that numerous applications exist for such high-bandwidth actuators including jet mixing, impingement noise suppression, and weapons bay applications.

## Acknowledgements

This work was funded by AFOSR under contract F49620-00-C-0046 under the program management of Dr. Steven Walker and Dr. John Schmisseur.

## References

[1] A.B. Cain, M.M. Rogers, V. Kibens, G. Raman, Simulations of high-frequency excitation of a plane wake, American Institute of Aeronautics and Astronautics 2001-0514, 2001.
[2] L. Kral, Active flow control technology, American Society of Mechanical Engineers Tech Brief, 1999.
[3] M. Gad-el-Hak, Flow Control: Passive, Active and Reactive Flow Management, Cambridge University Press, Cambridge, 2000.
[4] J.M. Wiltse, A. Glezer, Manipulation of free shear flows using piezoelectric actuators, Journal of Fluid Mechanics 249 (1993) 261–285.
[5] J.M. Wiltse, A. Glezer, Direct excitation of small-scale motions in free shear flows, Physics of Fluids 10 (8) (1998) 2026–2036.
[6] J. Hartmann, B. Troll, On a new method for the generation of sound waves, Physics Review 20 (1922) 719–727.
[7] J. Hartmann, On the production of acoustic waves by means of an air-jet of a velocity exceeding that of sound, Philosophical Magazine and Journal of Science XI (1931) 926.
[8] G. Raman, V. Kibens, A. Cain, J. Lepicovsky, Advanced actuator concepts for active aeroacoustic control, American Institute of Aeronautics and Astronautics Paper 2000-1930, 2000.

[9] G. Raman, A. Mills, S. Othman, V. Kibens, Development of powered resonance tube actuators for active flow control, American Society of Mechanical Engineers FEDSM 2001-18273, 2001.
[10] G. Raman, V. Kibens, Active flow control using integrated powered resonance tube actuators, American Institute of Aeronautics and Astronautics Paper 2001–3024, 2001.
[11] A.B. Cain, Private Communication on the use of high frequency excitation to suppress flow induced resonance, 1997.
[12] M. Stanek, G. Raman, V. Kibens, J. Ross, J. Peto, J. Odedra, Cavity tone suppression using high frequency excitation, American Institute of Aeronautics and Astronautics Paper 2000–1905, 2000.
[13] M.C. Thompson, K. Hourigan, M.C. Welsh, E. Brocher, Acoustic sources in a tripped flow past a resonator tube, American Institute of Aeronautics and Astronautics Journal 30 (6) (1992) 1484–1491.
[14] E. Brocher, C. Maresca, M.H. Bournay, Fluid dynamics of the resonance tube, Journal of Fluid Mechanics 43 (2) (1970) 369–384.
[15] J. Iwamoto, Experimental study in a rectangular jet-driven tube, Transactions of the American Society of Mechanical Engineers Journal of Fluids Engineering 112 (1) (1990) 23–27.
[16] J. Iwamoto, B.E.L. Deckker, A study of the Hartmann–Sprenger tube using the hydraulic analogy, Experiments in Fluids 3 (1985) 245–252.
[17] J. Wilson, An Investigation of Resonance Tubes, Master of Aeronautical Engineering Thesis, Cornell University, Graduate School of Aeronautical Engineering, Ithaca, NY, 1958.
[18] J. Wilson, E.L. Resler Jr., A mechanism of resonance tubes, Aerospace Sciences Reader's Forum Journal 26 (7) (1959).
[19] V. Kibens, Discrete noise spectrum generated by an acoustically excited jet, American Institute of Aeronautics and Astronautics Journal 18 (4) (1980) 434–441.
[20] G. Raman, E. Envia, T.J. Bencic, Jet cavity interaction tones, American Institute of Aeronautics and Astronautics Journal 40 (8) (2002) 1503–1511.
[21] E.J. Kerschen, Analytical modeling of the resonant frequencies of a powered resonance tube, Division of Fluid Dynamics of the American Physical Society Meeting, Nov. 18–20, San Diego, CA, 2001.
[22] J. Kastner, M. Samimy, Development and Characterization of Hartmann Tube Based Fluidic Actuators for High Speed Flow Control, American Institute of Aeronautics and Astronautics Paper 2002-0128, 2002.
[23] A.B. Cain, W.W. Bower, Proceedings of the Computational Aeroacoustics Workshop (NASA Langley), 1995 Comparison of spatial numerical operations for duct-nozzle acoustics.
[24] R.D. Blevins, Applied Fluid Dynamics Handbook, Van Nostrand Reinhold, New York, 1984.